

ENSO and non-ENSO induced charging and discharging of the equatorial Pacific

Bruce T. Anderson · Renellys C. Perez

Received: 6 June 2014 / Accepted: 7 January 2015
© Springer-Verlag Berlin Heidelberg 2015

Abstract It is well established that variations in extratropical North Pacific wind stress fields can influence the state of the tropical Pacific 12–15 months prior to the maturation of boreal winter El Niño/Southern Oscillation (ENSO) events. While most research has focused on accompanying variations in the North Pacific trade winds and underlying sea surface temperatures that subsequently shift equatorward via anomalous air–sea interactions—e.g. meridional mode dynamics—observational and numerical model analyses indicate empirical and dynamical links exist between these same trade-wind variations and concurrent changes in *subsurface* temperatures across the equatorial Pacific, which can also serve as a key initiator of ENSO events. This paper shows that within an observationally-constrained ocean reanalysis dataset this initiation mechanism—termed the trade-wind charging (TWC) mechanism—is induced by the second leading mode of boreal winter zonal wind stress variability over the tropical Pacific and operates separately from ENSO-induced recharge/discharge of the equatorial Pacific heat content. The paper then examines the characteristics and evolution of the ENSO and

TWC modes. Results indicate that the oceanic evolution for both modes is consistent with wind stress induced vertically-integrated, meridional mass transport into and out of the equatorial Pacific—i.e. a charging and discharging of the equatorial Pacific—despite having distinctly different wind stress anomaly patterns. The process-based similarity between these two modes of tropical Pacific wind stress variability suggests that both can produce a charging/discharging of the equatorial Pacific, however one (the ENSO mode) represents part of the ENSO cycle itself and the other (the TWC mode) represents a separate forcing mechanism of that cycle.

Keywords ENSO · Tropical–extratropical interactions · Ocean reanalysis · Charging and discharging processes · ENSO precursors

1 Introduction

The El Niño/Southern Oscillation (ENSO), with its concomitant changes in sea-surface temperatures (SSTs) across the equatorial Pacific, provides significant forcing of large-scale atmospheric circulations (Trenberth et al. 1998; Alexander et al. 2002) and influences both local and remote climates (Ropelewski and Halpert 1986, 1996; Kiladis and Diaz 1989; Ely et al. 1993; Gershunov and Barnett 1998; Schneider and Steig 2008), particularly during hemispheric winter (Kumar and Hoerling 1998; Shukla et al. 2000; Zheng et al. 2000). Although traditionally defined as an equatorial Pacific mode of coupled ocean/atmosphere variability (Philander 1985), numerous additional precursors to ENSO events are found in the subtropics/extratropics (Kidson 1975; Trenberth 1976; Reiter 1978; Rasmusson and Carpenter 1981; van Loon and Shea 1985, 1987; Barnett 1985; Trenberth and Shea 1987; Gu and Philander 1997;

B. T. Anderson (✉)
Department of Earth and Environment, Boston University,
Boston, MA 02215, USA
e-mail: brucea@bu.edu

B. T. Anderson
The Frederick S. Pardee Center for the Study of the
Longer-Range Future, Boston University, Boston,
MA 02215, USA

R. C. Perez
Cooperative Institute of Marine and Atmospheric Studies,
University of Miami, Miami, FL, USA

R. C. Perez
Atlantic Oceanographic and Meteorological Laboratory, NOAA,
Miami, FL, USA

Li 1997; Lynse et al. 1997; Barnett et al. 1999; Chan and Xu 2000; Pierce et al. 2000; Anderson 2003, 2004; Vimont et al. 2003a; Wang et al. 2012), suggesting that extratropical processes play an important role in forcing ENSO variability.

While various extratropical mechanisms for forcing ENSO have been proposed, our focus will be on boreal-winter near-surface circulations linked to the North Pacific Oscillation (NPO, the Pacific analogue to the NAO—Walker and Bliss 1932; Rogers 1981; Linkin and Nigam 2008), which via its influence on sea-level pressure (SLP) variations over the Hawaiian region is known to play a pivotal role in initiating the development of warm (i.e. El Niño) and cold (i.e. La Niña) ENSO events (Trenberth and Shea 1987; Barnett et al. 1988; Vimont et al. 2001; Anderson 2003). Over the last decade, most studies of these boreal-winter near-surface atmospheric circulations and their influence on the ENSO have highlighted the anomalous air–sea interactions that accompany them. These include the “Seasonal Footprinting Mechanism” whereby the atmospheric circulations establish underlying subtropical/tropical SST anomalies by spring, which persist until summer and subsequently sustain SLP and wind stress anomalies that are conducive to initiating ENSO events (Vimont et al. 2001, 2003a, b). They also include the Pacific “Meridional Mode” (MM) mechanism whereby the atmospheric circulations, through their influence on the trade winds, produce an equatorward migration of underlying SSTs via the wind–evaporation–SST (WES) feedback (Xie 1999), resulting in the disturbance of equatorial SSTs and onset of ENSO events (Chiang and Vimont 2004; Chang et al. 2007; Zhang et al. 2009; Alexander et al. 2010; Wu et al. 2010; Larson and Kirtman 2013).

However recent findings demonstrate that these same near-surface atmospheric circulations can directly force *subsurface* heat content changes across the central equatorial Pacific—a well-known precursor to mature ENSO events (Wyrтки 1985; Jin 1997; Meinen and McPhaden 2000; Newman et al. 2011; Wen et al. 2014)—via their influence on trade-wind induced vertically-integrated, meridional mass transport, resulting in a “trade wind charging” (TWC) of the equatorial Pacific (Anderson et al. 2013a, b). Indeed, NPO-related subsurface heat content changes have been noted in observational (Anderson 2004) and reanalysis (Anderson et al. 2013a, b) data as well as coarse-scale (Anderson and Maloney 2006; Alexander et al. 2010) and eddy permitting (Anderson et al. 2013a, b) numerical models.

It is important to note, though, that trade-wind induced vertically-integrated mass transport into (and out of the) equatorial Pacific is not uniquely related to NPO-induced boreal-winter near-surface atmospheric circulations. Indeed, it is central to the recharge–discharge mechanism for sustaining the oscillatory behavior of the ENSO cycle, as envisioned by Jin (1997) and elucidated in Clarke et al.

(2007). Since the dynamical process for each mechanism (i.e. the trade-wind charging mechanism and the recharge–discharge mechanism) involves variations in the equatorial and off-equatorial trade winds over the Pacific and, via their curl, equatorial ocean heat content, we will refer to the process itself as charging (resulting in a positive subsurface temperature anomaly) and discharging (resulting in a negative subsurface temperature anomaly) of the equatorial Pacific heat content. A key motivation of this study, then, is to explicitly isolate the wind stress fields and subsurface heat content changes linked to the oscillatory ENSO cycle *vis a vis* those linked to TWC initiation of ENSO events. Once isolated we want to characterize the coupling between the atmosphere and underlying ocean as it relates to the charging and discharging of the equatorial Pacific by each mechanism.

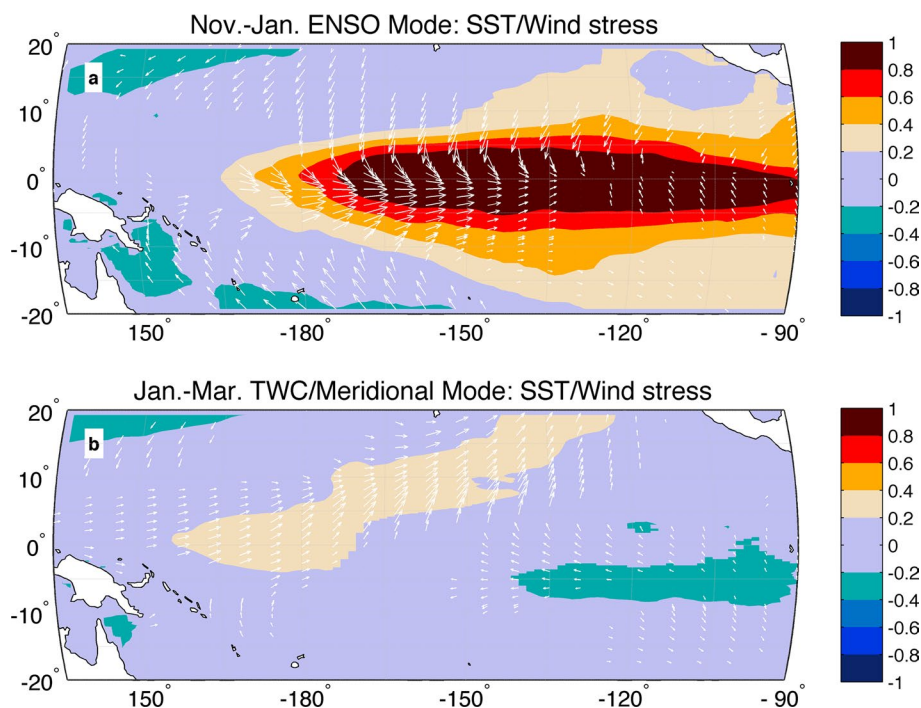
Specifically, Sect. 2 presents an overview of the data and statistical methods employed to identify the leading modes of boreal winter zonal wind stress variability over the tropical Pacific. The characteristic atmospheric and oceanic structures of these modes are then presented in Sect. 3. Further, this section examines the evolution of these atmospheric and oceanic structures both at the surface and beneath it, as well as their co-evolution. Discussion of the results and implications for oscillatory and forced behavior of the tropical Pacific follow in Sect. 4.

2 Data and methods

2.1 Data

For this study, we use atmospheric and oceanic fields taken from the observationally-constrained ORA-S3 European Centre for Medium-Range Weather Forecasts (ECMWF) ocean reanalysis (Balmaseda et al. 2008), including wind stress, surface and subsurface ocean temperatures, oceanic heat content represented by the vertically-averaged temperature anomalies integrated from 0 to 300 m, and meridional velocity anomalies. These data extend from 1959 to 2006 with monthly time resolution and 1° spatial resolution off the equator tapering to 0.3° (in the meridional direction) at the equator. Assimilated data include surface and subsurface temperature and salinity (through 2,000 m) along with sea-level heights, all of which are quality controlled and bias-corrected prior to assimilation. Surface flux forcing (wind stress; freshwater; heat) are provided by modified fields taken from the 40-yr ECMWF Reanalysis (ERA-40) for 1959–2002 and from the ECMWF operational analyses after that. These are then used to force an ocean-only model (the Hamburg Ocean Primitive Equation model—HOPE) in order to obtain a first-guess of the ocean state, at which point the bias-corrected observational data are assimilated;

Fig. 1 **a** Tropical Pacific ocean/atmosphere anomalies regressed against the leading mode of boreal winter τ^x variability—see text for details. *Shading* seasonal-mean (Nov–Jan) sea-surface temperature (SST) anomalies regressed against the concurrent τ^x time-series. Contour interval is $0.2\text{ }^\circ\text{C}$; minimum contour is $\pm 0.2\text{ }^\circ\text{C}$. Only significant ($p < 0.10$ based upon a two-tailed t test) values are shown. Vectors seasonal-mean wind stress anomalies (N m^{-2}) regressed against the τ^x time-series. Only vectors with significant ($p < 0.10$) anomalies in magnitude are shown. **b** Same as **a** except for the Jan–Mar SST and wind stress anomalies regressed against the concurrent time-series for the second leading mode of boreal winter τ^x variability



further, five separate analyses, forced by five different perturbed wind stress fields, are produced in order to arrive at an ensemble estimate of the three-dimensional state of the ocean and its time evolution. Full details about this data product and its evaluation against observations and previous analysis products can be found in Balmaseda et al. (2008). In addition, its evaluation against more recent analysis products (i.e. the ORA-S4—Balmaseda et al. 2013) indicates that because of the observationally-constrained nature of these products they show similar behavior over the tropical Pacific, despite having different assimilation and numerical modeling systems.

2.2 Methods

Since our interest is in identifying atmospheric processes that give rise to the charging and discharging of equatorial Pacific heat content, we first determine the leading modes of variability in the tropical wind stress fields over the Pacific. Adopting the same method and domain used in Larson and Kirtman (2013), we apply an Empirical Orthogonal Function (EOF) analysis to the zonal winds stress fields (hereafter, τ^x) between 15°S and 15°N , 160°E and 80°W . Here we apply it to the year-to-year variations in the seasonal-mean fields found during extended boreal winter (November–March) when both the ENSO variations are largest (November–January—Jin et al. 1994; Trenberth 1997) and the MM and TWC precursors to ENSO variability are also highly active (January–March—Chiang and Vimont 2004; Chang et al. 2007). One crucial difference

with the application here, vis a vis that employed by Larson and Kirtman (2013), is that we chose not to preprocess the anomalies by first removing the ENSO-related components. The reason for doing so is that we wish to analyze not just the non-ENSO related components, but also compare and contrast them with the ENSO-related components themselves so as to better understand how modes of atmospheric variability in the Pacific, and the underlying oceanic responses, are related and how they may differ.

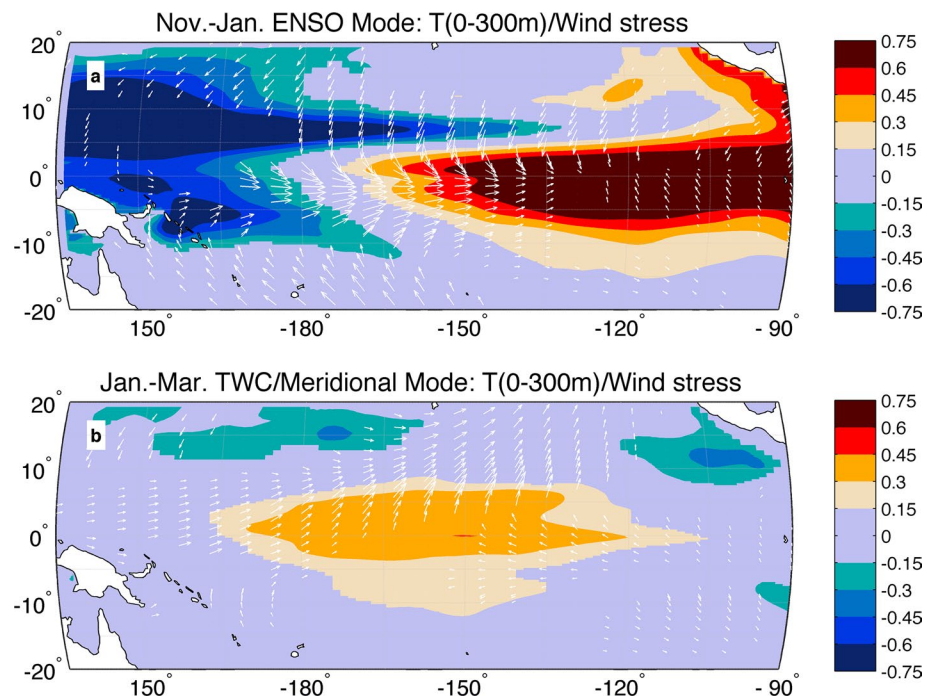
3 Results

3.1 Seasonal mean fields

The leading mode of boreal winter zonal wind stress variability is associated with ENSO variability (Fig. 1a). It is characterized by large positive SST anomalies extending across the central and eastern equatorial Pacific and significant westerly wind stress anomalies over the central portion of the basin, with additional off-equatorial northeasterly (southeasterly) anomalies over the western portion of the North (South) Pacific. Given its spatial and temporal relation with ENSO variability ($r = 0.91$ between the first τ^x principal component—PC—time-series and the concurrent Nov.-Jan. Niño-3 index), we label this leading mode of variability the “ENSO” mode.

As will be shown, the second leading mode of boreal winter zonal wind stress variability over the tropical Pacific is associated with TWC/MM variations (Fig. 1b). This

Fig. 2 **a** Shading seasonal-mean (Nov–Jan) T (0–300 m) anomalies ($^{\circ}\text{C}$) regressed against the concurrent time-series for the leading mode of boreal winter τ^x variability. Contour interval is $0.15\text{ }^{\circ}\text{C}$; minimum contour is $\pm 0.15\text{ }^{\circ}\text{C}$. Only significant ($p < 0.1$ based upon a two-tailed t test) values are shown. *Vectors* same seasonal-mean wind stress anomalies as in Fig. 1a. **b** Same as **a** except for the Jan–Mar T (0–300 m) and wind stress anomalies regressed against the concurrent time-series for the second leading mode of boreal winter τ^x variability



mode is characterized by significant westerly anomalies over the western equatorial Pacific and easterly anomalies over the eastern equatorial Pacific. In addition, significant wind stress variations extend into the subtropics of the North Pacific, with a southwesterly orientation. Not surprisingly, these wind stress variations are similar to those associated with the leading mode of “atmospheric noise” in the tropical Pacific (once the ENSO-related component has been linearly removed—Larson and Kirtman 2013), which in turn have been linked to the MM. Indeed, the τ^x PC time-series isolated through this analysis is highly positively correlated ($r = 0.84$) with concurrent January–March MM-related 10 m wind fields (as derived in Chiang and Vimont 2004 and archived at the NOAA/ESRL monthly climate indices website) and negatively correlated ($r = -0.79$) with concurrent subtropical sea-level pressure variations (as captured by the Hawaiian Sea-level Pressure Index, HSLPI, derived by Anderson 2003), both of which serve as significant precursors to ENSO variations 12–15 months later (e.g. Anderson 2003; Chang et al. 2007). As expected positive SST anomalies extend northeastward into the central and eastern North Pacific with negative SST anomalies in the eastern South Pacific, characteristic of the MM SST signature, as well as the optimal initial SST structure that precedes ENSO events by 7–9 months (Penland and Sardeshmukh 1995; Penland 1996).

As highlighted in the Sect. 1, however, subsurface temperatures can also be influenced by equatorial and off-equatorial wind stress variations (not just in the Pacific but also the Atlantic—Richter et al. 2013). As such we perform a

similar regression analysis with concurrent depth-averaged 0–300 m temperature anomalies that serve as a proxy for heat content anomalies (Fig. 2). The ENSO mode of wind stress variability is associated with a dipole in heat content anomalies across the tropical Pacific in which the eastern lobe is co-located with the temperature anomalies at the surface (cf. Figure 5a, c from Kug et al. 2003). By contrast, the MM/TWC mode of wind stress variability is associated with positive heat content anomalies primarily between 165°E – 120°W and 10°S – 7.5°N that extend to 110°W along the equator. These extensive subsurface temperature anomalies spanning the tropical Pacific are structurally similar to a charging of the warm-water volume across the equatorial Pacific that serves as a precursor to mature El Niño events (Meinen and McPhaden 2000; McPhaden 2003; Newman et al. 2011).

Recognizing the similarity between the wind stress and SST anomalies associated with the second τ^x PC time-series (Fig. 1b) and those previously documented for the MM (e.g. Chiang and Vimont 2004), it is of interest to see whether the subsurface anomalies are also similar. As expected, both the second τ^x PC time-series isolated here and the MM-related 10 m wind time-series derived from the Chiang and Vimont (2004) analysis (and archived at the NOAA/ESRL monthly climate indices website) have similar wind stress and SST anomalies associated with them, both off the equator and along it (Fig. 3). Given the similarity in the wind stress fields, it is not surprising to find that the T(0–300 m) anomalies related to the second τ^x PC time-series and the MM-related 10 m wind time-series also

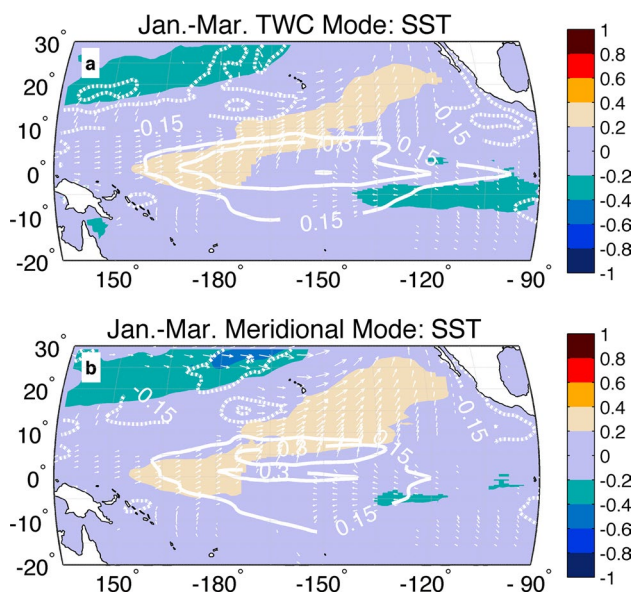


Fig. 3 **a** Shading and vectors same seasonal-mean sea-surface temperature and wind stress anomalies as in Fig. 1b. Contours same seasonal-mean T (0–300 m) anomalies as in Fig. 2b. **b** Same as **a** except for the SST, T (0–300 m) and wind-stress anomalies regressed against the concurrent seasonal-mean (Jan–Mar) 10 m wind time-series for the Pacific Meridional Mode, as found on the NOAA/ESRL monthly climate indices site (<http://www.esrl.noaa.gov/psd/data/timeseries/monthly/PMM/>)

have very similar structures both along the equator and off of it. However, because the second τ^x PC time-series tends to be more strongly related to lower-latitude wind-stress anomalies vis a vis the MM-related 10 m wind time-series, the second τ^x PC time-series tends to have larger amplitude T(0–300 m) anomalies (but weaker subtropical SST anomalies) associated with it (cf. Fig. 3a, b).

These results confirm that while the MM technically refers to “an anomalous SST gradient across the mean latitude of the ITCZ” (as defined in Chiang and Vimont 2004), there are additional related (subsurface) oceanic perturbations that have gone largely unanalyzed. Indeed, the relation of the wind-stress variations with these subsurface temperature anomalies tends to be larger than with the SSTs, based both upon the relative magnitude of the corresponding SST and T(0–300 m) anomalies compared to the ENSO-related variations in Figs. 1, 2 respectively (see also Figs. 9, 12 below), as well as upon their respective zero-lag correlations with the zonal wind stress time series (which never exceed $r = 0.6$ for the SST fields, but consistently reach $r > 0.7$ across the core of the subsurface heat content anomalies and even exceed $r = 0.8$ along the off-equatorial branch). As such, although the wind stress anomalies associated with the 2nd leading mode of zonal wind stress variability discussed here are functionally equivalent to those that influence MM-related SSTs, in this paper we will

instead refer to this mode of tropical wind stress variability as the “TWC” mode.

Having isolated the two leading modes of tropical Pacific wind stress variability, it is now of interest to diagnose how they may be dynamically coupled to the underlying subsurface temperatures. To begin, zonal wind stress anomalies associated with the ENSO mode have a very characteristic monopole structure centered on the dateline, with positive (westerly) values at or just south of the equator that decrease towards higher latitudes (Fig. 4a), nearly identical to those associated with ENSO itself (cf. Figure 3 from Clarke et al. 2007). For the TWC mode (Fig. 4b), the positive zonal wind stress anomalies tend to be weaker than the ENSO-related anomalies, while along the equator there is a dipole structure with westerly (easterly) anomalies found to the west (east) of the subsurface temperature anomalies. In addition, east of the dateline westerly anomalies extend northeastward across the central tropical North Pacific north of the equatorial easterly anomalies, resulting in an off-equatorial wind stress curl that can produce both horizontal and vertical circulations within the underlying ocean.

Indeed, we can estimate the implied vertically-integrated meridional mass transport, V , associated with both of these modes based upon the curl of the wind stress anomalies and vortex stretching of the water columns (Clarke et al. 2007), such that:

$$V \approx \frac{(\partial\tau^y/\partial x - \partial\tau^x/\partial y)}{\beta\rho} + \frac{f}{\beta} \cdot \frac{\partial h_{15^\circ\text{C}}}{\partial t} \quad (1)$$

where V is the depth-integrated meridional velocity; τ^x and τ^y are the eastward and northward components of the wind stress, respectively; ρ is the density (here set to a representative value of $1,025 \text{ kg/m}^3$); β is the beta parameter; f is the Coriolis parameter; and $\frac{\partial h_{15^\circ\text{C}}}{\partial t}$ is the local vertical velocity at the base of the thermocline, here designated by the climatological depth of the 15°C isotherm (Capotondi et al. 2003; Deser et al. 2006, 2012; see also Figs. 9, 12). The first term on the r.h.s. of Eq. 1 captures the northward (southward) transport needed to balance changes in the warm water volume induced by a positive (negative) curl of the wind stress anomalies at the surface. The second term on the r.h.s. of Eq. 1 captures the poleward (equatorward) transport needed to balance changes in the warm water volume induced by positive (negative) vortex stretching at the base of the thermocline. Note, given the sign convention, a positive time derivative of this quantity corresponds to a deepening of the thermocline and a negative vertical velocity.

For the ENSO mode (Fig. 5a), implied poleward transport extends across the tropical Pacific and is associated with positive (negative) curl in the surface wind stress fields north (south) of the equator (cf. Figure 7 from

Fig. 4 **a** Shading seasonal-mean (Nov–Jan) τ^x anomalies regressed against the concurrent time-series for the leading mode of boreal winter τ^x variability. Contour interval is 0.003 (N m^{-2}); minimum contour is ± 0.003 (N m^{-2}). Only significant ($p < 0.1$ based upon a two-tailed t test) values are shown. *Contours* same seasonal-mean T (0–300 m) anomalies as in Fig. 2a. *Vectors* same seasonal-mean wind stress anomalies as in Fig. 1a. **b** Shading same as **a** except for the Jan–Mar τ^x anomalies regressed against the concurrent time-series for the second leading mode of boreal winter τ^x variability. *Contours* same seasonal-mean T (0–300 m) anomalies as in Fig. 2b. *Vectors* same seasonal-mean wind stress anomalies as in Fig. 1b

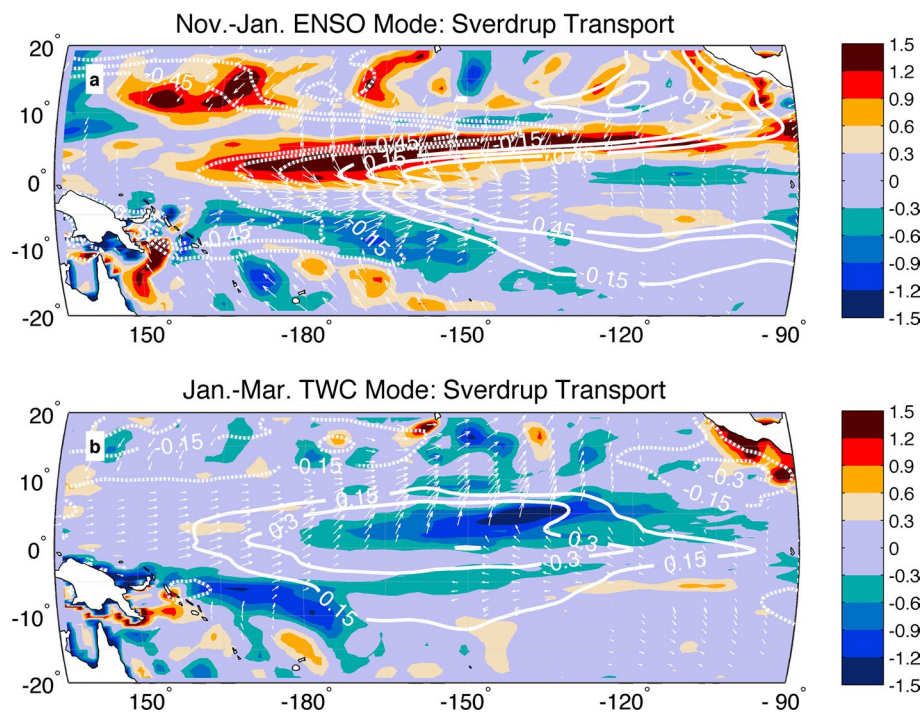
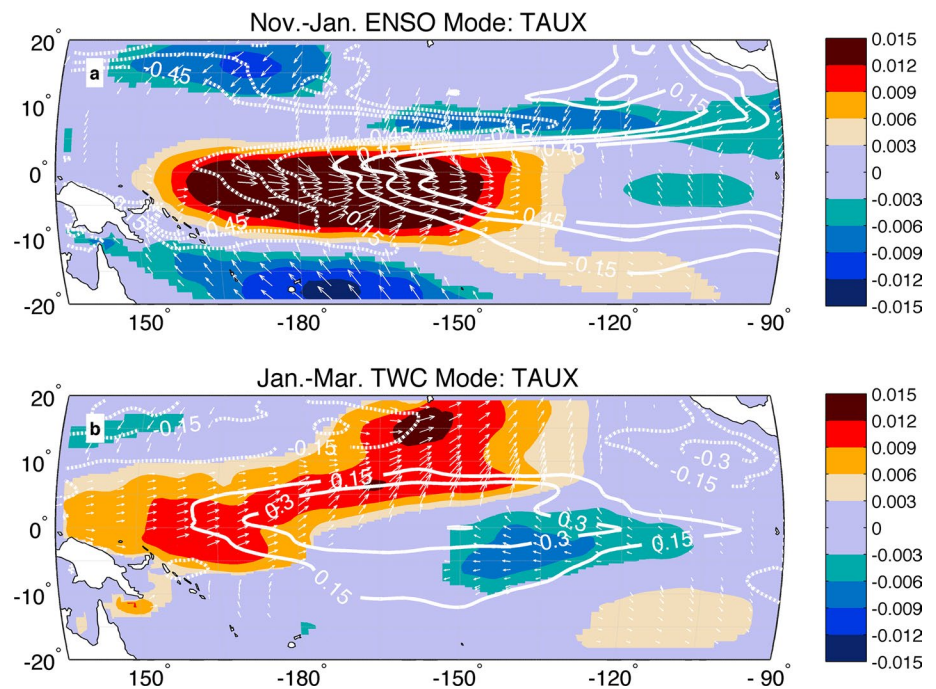
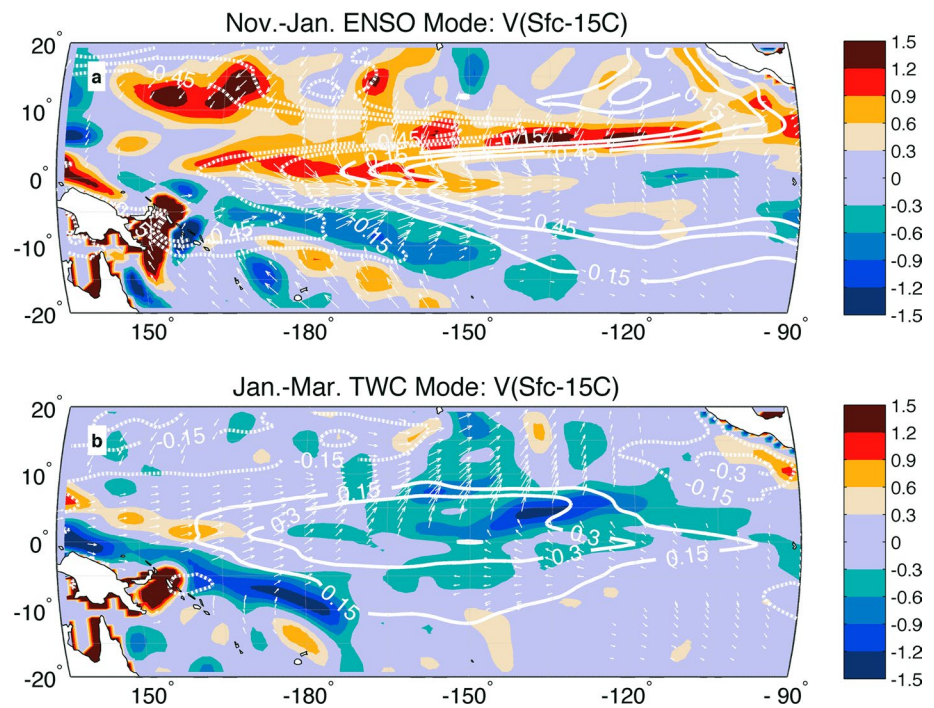


Fig. 5 **a** Shading the implied vertically-integrated meridional velocity component derived by applying Eq. 1 to the seasonal-mean (Nov–Jan) wind stress anomalies and vertical velocities at the 15 °C isotherm depth regressed against the concurrent time-series for the leading mode of boreal winter τ^x variability. Minimum shading is ± 0.3 $\text{m}^2 \text{s}^{-1}$; shading interval is 0.3 $\text{m}^2 \text{s}^{-1}$. *Contours* same seasonal-mean T (0–300 m) anomalies as in Fig. 2a. *Vectors* same seasonal-mean wind stress anomalies as in Fig. 1a. **b** Shading same

as **a** except for the implied vertically-integrated meridional velocity component derived by applying Eq. 1 to the seasonal-mean (Jan–Mar) τ^x anomalies and vertical velocities at the 15 °C isotherm depth regressed against the concurrent time-series for the second leading mode of boreal winter τ^x variability. *Contours* same seasonal-mean T (0–300 m) anomalies as in Fig. 2b. *Vectors* same seasonal-mean wind stress anomalies as in Fig. 1b

Fig. 6 **a** Shading seasonal-mean (Nov–Jan) vertically-integrated (Sfc–15 °C) meridional velocity anomalies regressed against the concurrent time-series for the leading mode of boreal winter τ^x variability. Minimum shading is $\pm 0.3 \text{ m}^2 \text{ s}^{-1}$; shading interval is $0.3 \text{ m}^2 \text{ s}^{-1}$. Contours same seasonal-mean T (0–300 m) anomalies as in Fig. 2a. Vectors same seasonal-mean wind stress anomalies as in Fig. 1a. **b** Shading same as **a** except for the Jan–Mar vertically-integrated (Sfc–15 °C) meridional velocity anomalies regressed against the concurrent time-series for the second leading mode of boreal winter τ^x variability. Contours same seasonal-mean T (0–300 m) anomalies as in Fig. 2b. Vectors same seasonal-mean wind stress anomalies as in Fig. 1b



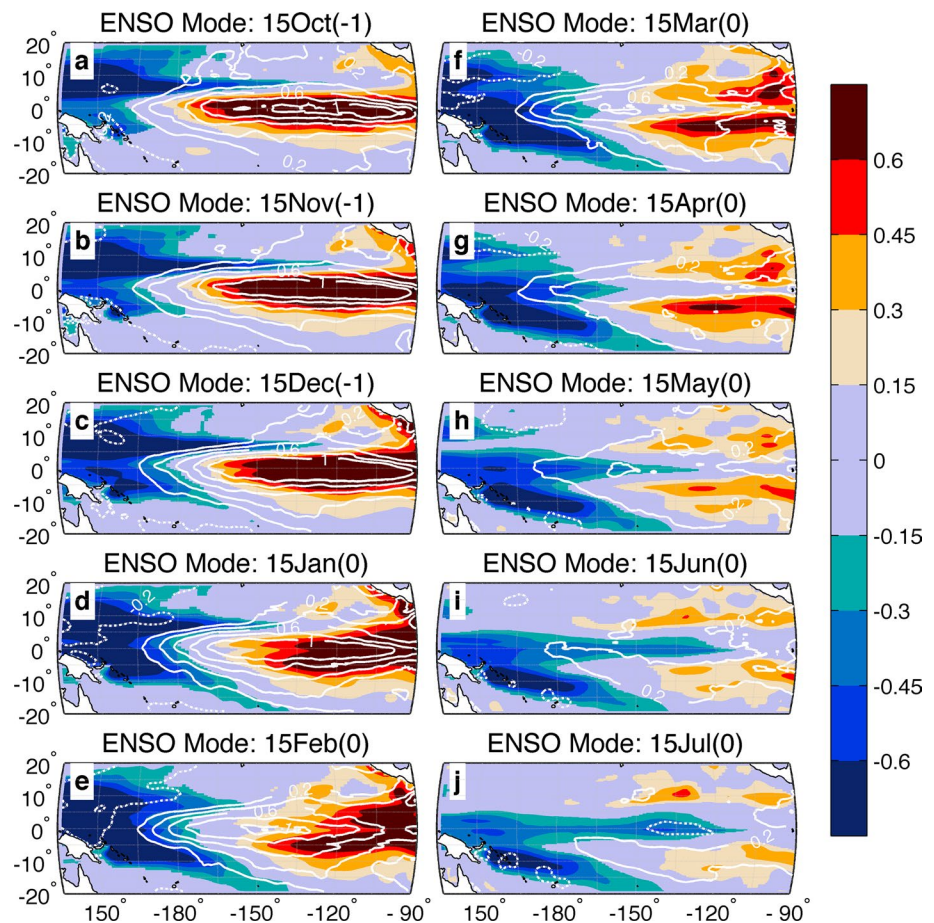
Clarke et al. 2007). However, equatorial divergence (leading to the discharge of water from the equatorial Pacific) is concentrated between 150°E and 150°W on either side of the equator, co-located with the strong horizontal gradients in the subsurface temperature anomalies. By contrast, for the TWC mode (Fig. 5b), the implied vertically integrated mass transport is predominantly equatorward and centered over the central portion of the basin, principally north of the equator, co-located with the maximum in subsurface temperature anomalies. Further examination of the two contributing terms in Eq. 1 indicates that near the equator the vertical displacements of the base of the thermocline (i.e. the second term on the r.h.s. of Eq. 1) between 5°S and 5°N are very small for the TWC-mode (not shown). This result suggests that the implied vertically-integrated meridional velocities between 5°S and 5°N for the TWC-mode are principally generated by the wind stress curl anomaly component (i.e. the first term on the r.h.s. of Eq. 1). In some regions (approximately east of 150°W) the negative wind stress curl that induces this transport arises from the meridional gradient between equatorial easterly anomalies and a weakening of the off-equatorial trade winds (i.e. westerly anomalies). The implied equatorward mass transport results in a charging of the equatorial Pacific at these longitudes and is co-located with an eastward extension of the equatorial heat content anomalies. However in other regions—particularly the region between 180° and 150°W where the positive heat content anomalies are largest—the curl results mainly from the weakening of the off-equatorial trade winds (given the absence of

any significant equatorial wind stress anomalies at these longitudes—cf. Fig. 4b).

It should be noted here that the curl in the wind stress not only gives rise to vertically-integrated meridional mass transport, but also to vertical displacements of the underlying water itself. In particular, for the TWC mode, the off-equatorial wind stress curl found at approximately 4°N tends to induce Ekman mass convergence and downwelling (not shown). The fact that the vertical circulations induced by this off-equatorial wind stress curl are co-located with the axis of off-equatorial heat-content anomalies in the North Pacific suggests that wind-induced vertical motions may be contributing to the anomalous subsurface temperature structure associated with this mode as well.

To confirm that the implied vertically-integrated mass transport described above is a valid approximation for the response of the ocean, we examine the depth-integrated meridional currents estimated from the ocean analysis itself. For consistency, we integrate these currents from the surface to the base of the (local) thermocline, again designated by the climatological depth of the 15°C isotherm (Fig. 6). Overall, the vertically-integrated meridional currents concurrent with the ENSO mode bear a strong resemblance, both in structure and magnitude, to the implied currents derived from the curl of the wind stress fields and vortex stretching (cf. Figs. 5a, 6a), albeit with slightly weaker northward transport over the western tropical Pacific. For the TWC mode, the correspondence between the calculated and implied vertically-integrated meridional currents is also good (Figs. 5b, 6b), although again it tends

Fig. 7 The evolution of the tropical Pacific ocean/atmosphere system concurrent with and following wind stress variations associated with the ENSO mode of variability. *Shading* monthly-mean T (0–300 m) anomalies ($^{\circ}\text{C}$) regressed against the time-series for the leading mode of boreal winter τ^x variability. Shading interval is 0.15°C ; minimum shading is $\pm 0.15^{\circ}\text{C}$. Only significant ($p < 0.1$ based upon a two-tailed t test) values are shown. *Contours* monthly-mean T (5 m) anomalies ($^{\circ}\text{C}$) regressed against the τ^x time-series. Contour interval is 0.2°C ; minimum contour is $\pm 0.2^{\circ}\text{C}$. **a–j** Monthly-mean regression fields centered on 15 October prior to the boreal winter ENSO mode time-series through 15 July following the boreal winter ENSO mode time-series



to be somewhat weaker than implied in the central tropical Pacific. That said, because our interest is in the dynamical process of charging and discharging of the equatorial Pacific, which is explicitly tied to the wind stress anomalies and their curl, we will continue to analyze these fields to determine their relevance to changes in the vertically-integrated temperatures (i.e. heat content) along the equatorial Pacific.

3.2 Time evolution

3.2.1 ENSO mode

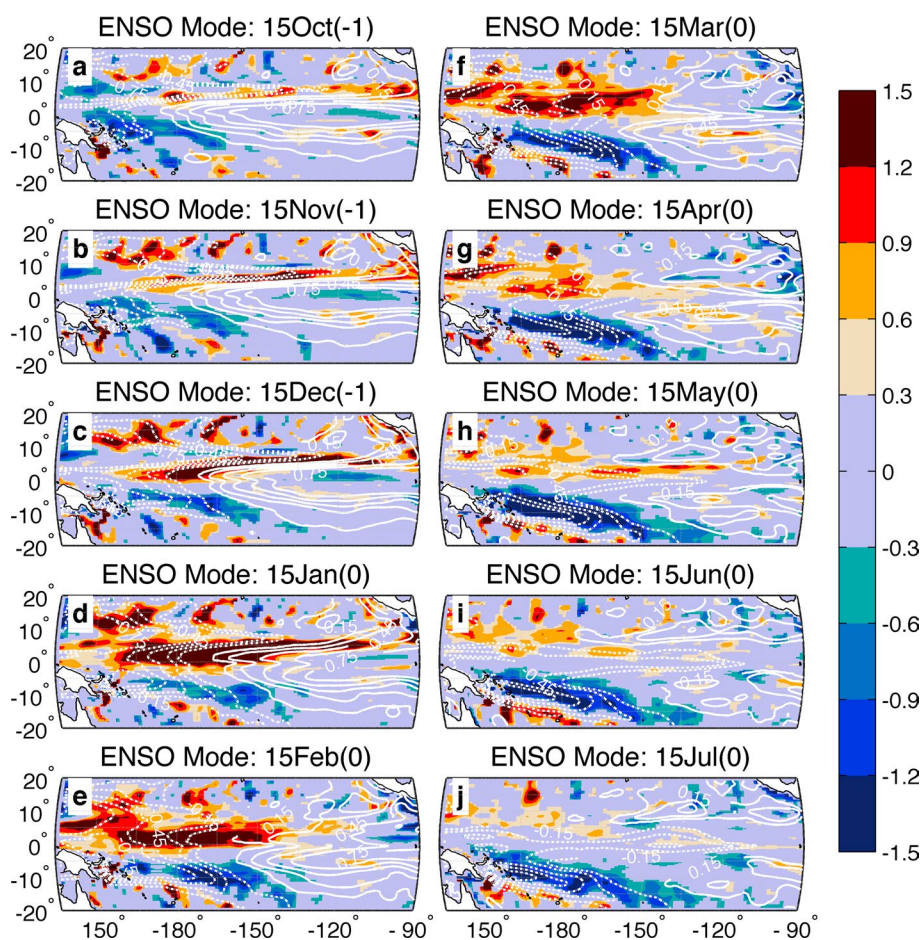
The motivating interest for this research is not to simply characterize the structure of the atmosphere and underlying ocean associated with the leading modes of near-surface wind stress forcing, but understand how these structures evolve over time, particularly as this evolution relates to the charging and discharging of the equatorial Pacific. To start, we examine the monthly-mean heat content and SST anomalies concurrent with and following the first leading mode of covariability (i.e. the ENSO mode—Fig. 7). While the evolution of these fields is well documented (e.g. Ishida et al. 2008; Kao and Yu 2009), we present it here so as to

compare it with the evolution of similar fields in response to the TWC mode discussed next.

Prior to boreal winter (Fig. 7a, b), the typical surface and subsurface temperature anomalies associated with the positive (El Niño) phase are already well established, as are the overlying wind stress fields (not shown). While the SST and wind stress anomalies remain fairly constant through most of the early winter (December—Fig. 7c), the subsurface temperature anomalies over the central equatorial Pacific begin to weaken such that by February (Fig. 7e) there is a local minimum in equatorial subsurface temperature anomalies extending across the basin, which continues to develop. Interestingly, despite this minimum in equatorial subsurface temperature anomalies, the SST anomalies continue to show local maxima along the equator until May (Fig. 7h). Starting in March the SST anomalies weaken substantially and essentially dissipate by June (Fig. 7i) while the negative subsurface temperatures anomalies that had been generated along the equator (as well as in the western Pacific) extend across the basin, resulting in a discharged equatorial Pacific that eventually influences the overlying SSTs in the eastern equatorial Pacific (Fig. 7j).

To better understand this evolution, particularly of the subsurface temperature anomalies, we examine the

Fig. 8 The evolution of the implied vertically-integrated meridional velocity component concurrent with and following wind stress variations associated with the ENSO mode of variability. *Shading* monthly-mean implied vertically-integrated meridional velocity component derived by applying Eq. 1 to the monthly-mean wind stress anomalies and vertical velocities at the 15 °C isotherm depth regressed against the time-series for the leading mode of boreal winter τ^x variability. Minimum shading is $\pm 0.3 \text{ m}^2 \text{ s}^{-1}$; shading interval is $0.3 \text{ m}^2 \text{ s}^{-1}$. *Contours* same monthly-mean T (0–300 m) anomalies as in Fig. 7. **a–j** Monthly-mean regression fields centered on 15 October prior to the boreal winter ENSO mode time-series through 15 July following the boreal winter ENSO mode time-series

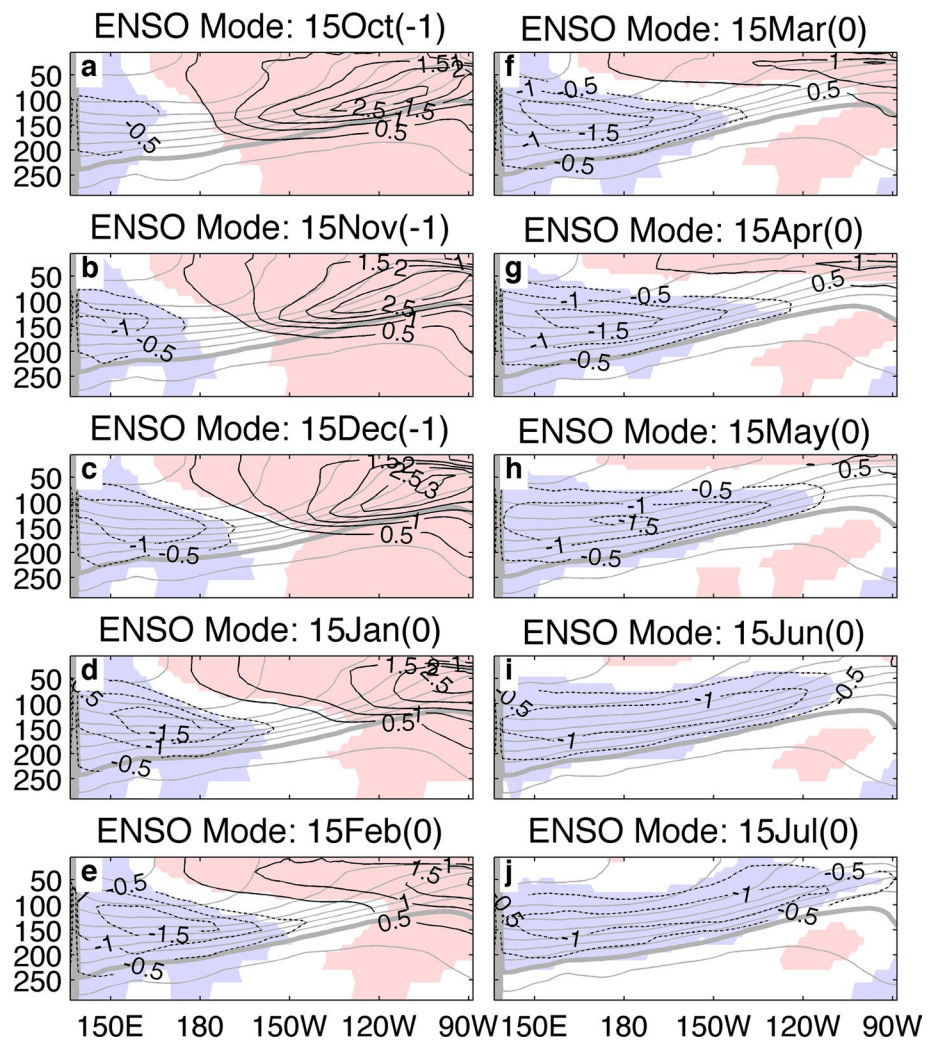


evolution of the implied vertically-integrated meridional mass transport based upon the curl of the wind stress anomalies and vortex stretching (Fig. 8). As with the seasonal mean fields, at the start of boreal winter, significant poleward vertically-integrated mass transport extends across the western and central tropical Pacific, particularly north of the equator. However, the largest transport off the equator, and hence equatorial divergence, does not occur until December/January (Fig. 8c, d). This equatorial divergence and resultant discharge in turn is co-located with the initial decreases in equatorial subsurface temperature anomalies. The off-equatorial discharge of heat persists through March (Fig. 8f) and remains co-located with the local minimum in subsurface temperature anomalies on and off the equator. As the off-equatorial transport begins to dissipate in April (Fig. 8g), the negative subsurface temperature anomalies, which until this point had been confined to the west of the dateline, extend across the equatorial Pacific (Fig. 8h–j), culminating in a discharged equatorial basin discussed above.

To see the characteristic equatorial response of the subsurface temperatures to the overlying wind stress anomalies and implied vertically-integrated meridional mass

transport, we next look at their evolution along an equatorial transect of the Pacific (Fig. 9). Initially, the equatorial Pacific is dominated by positive anomalies, which are at a maximum along the thermocline. However over the far western Pacific, cold water anomalies start to develop, most likely in response to the accumulated effect of westward propagating Rossby waves (cf. Fig. 7a). During the peak of the ENSO event (November/December) the subsurface warm water anomalies continue to persist over the eastern half of the basin (Fig. 9b, c). In the western half, however, cold water anomalies intensify, particularly between 150°E and 180°E in the region where the initial poleward transport along the equator develops. From January to March (Fig. 9d, f)—the period with largest off-equatorial mass transport (i.e. discharge)—the negative subsurface temperature anomalies expand eastward to 150°W, but their core stays relatively stationary through this 3-month period. In April (Fig. 9g)—corresponding to the time when the associated wind stress fields begin to dissipate along with the wind stress forcing of the meridional mass transport—the cold water anomaly extends eastward along the shoaling thermocline, effectively eroding the SST anomalies over the eastern equatorial Pacific approximately 2 months

Fig. 9 The evolution of the surface and subsurface temperature anomalies along the equatorial Pacific (2°S – 2°N) concurrent with and following wind stress variations associated with the ENSO mode of variability. *Black contours* monthly-mean temperature anomalies ($^{\circ}\text{C}$) regressed against the time-series for the leading mode of boreal winter τ^x variability. Contour interval is 0.5°C ; minimum contour is $\pm 0.5^{\circ}\text{C}$. *Shading* location of significant temperature anomalies ($p < 0.1$ based upon a two-tailed t test). *Grey contours* climatological isotherms. For reference, the 15°C isotherm is shown by the *thick grey line*; climatological isotherms contoured every 2.0°C . **a–j** Monthly-mean regression fields centered on 15 October prior to the boreal winter ENSO mode time-series through 15 July following the boreal winter ENSO mode time-series



later (i.e. by June) and producing negative SST anomalies in the eastern equatorial Pacific (Fig. 9j).

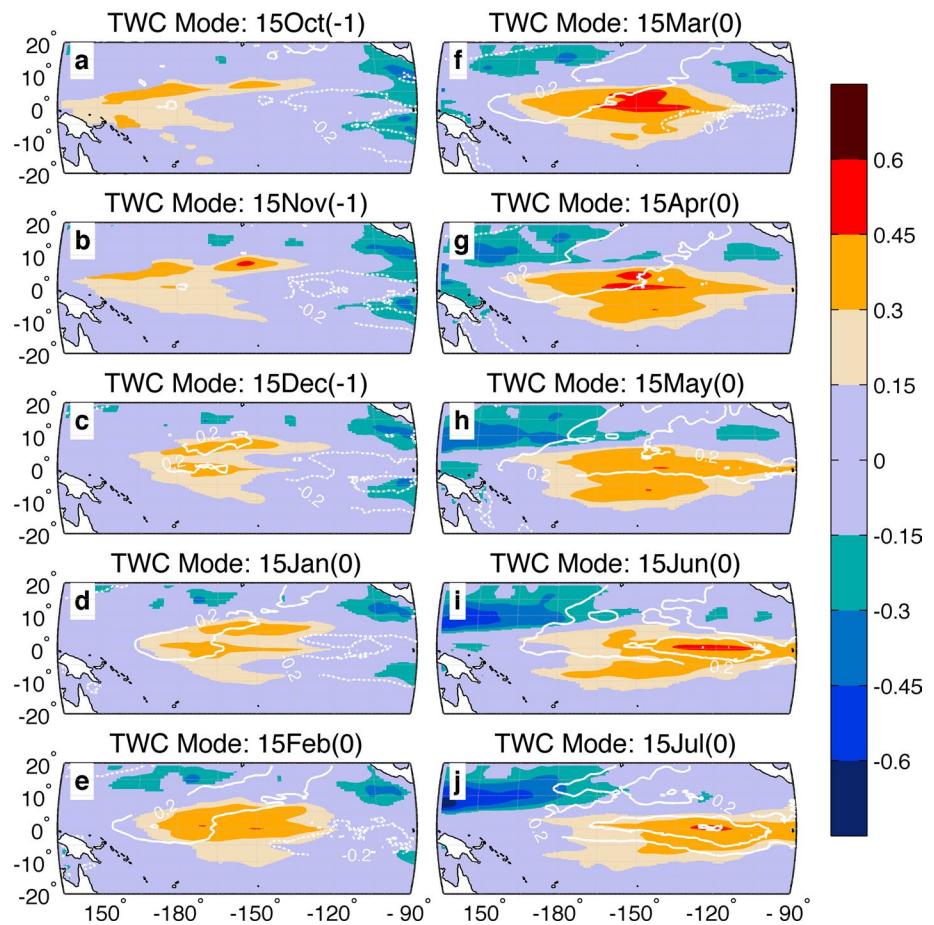
3.2.2 TWC mode

We now examine the characteristic evolution of the TWC mode, starting with the monthly-mean heat content and SST anomalies (Fig. 10). Prior to boreal winter, there are initial off-equatorial wind stress anomalies in both the northern and southern hemispheres, representative of a weakening of the trade-winds in these regions (not shown). Equatorward of these trade wind anomalies are positive off-equatorial subsurface heat content anomalies extending across much of the western and central Pacific (principally in the North Pacific—Fig. 10a, b). Positive (negative) subsurface heat content anomalies are also found along the equator over the western (far eastern) Pacific. By December and January (Fig. 10c, d), the positive subsurface temperature anomalies have intensified both along the equator and off of it; by contrast, there are still no substantial positive

SST anomalies present either along the equator or in the off-equatorial region to the north. By February and March (Fig. 10e, f), subsurface heat content anomalies and surface SST anomalies (as well as the wind stress anomalies—not shown) resemble the seasonal-mean fields themselves and are characterized by the establishment of extensive positive subsurface temperature anomalies extending from 150°E to 120°W and 5°S to 5°N along with positive SST anomalies that span from the western equatorial Pacific to the eastern subtropical North Pacific.

Moving into April the positive SST anomalies (representative of the MM) and positive subsurface temperature anomalies (representative of the TWC) continue to persist (Fig. 10g). In addition, the equatorial subsurface temperature anomalies continue to extend eastward over time. Interestingly, however, the positive SST anomalies off the equator remain relatively stationary, as do those at the equator in the western Pacific. Indeed, it is not until May (Fig. 10h) that positive SST anomalies extend across the equatorial Pacific. These in turn are co-located with the underlying

Fig. 10 Same as Fig. 7 except now for the evolution of the SST and T (0–300 m) anomalies concurrent with and following wind stress variations associated with the TWC mode of variability as represented by the time-series for the second leading mode of boreal winter τ^x variability



subsurface temperature anomalies (but dislocated from the off-equatorial SST anomalies over the North Pacific) such that both the surface and subsurface temperature anomalies develop local maxima around 140°W – 110°W over the course of the following months (Fig. 10i, j).

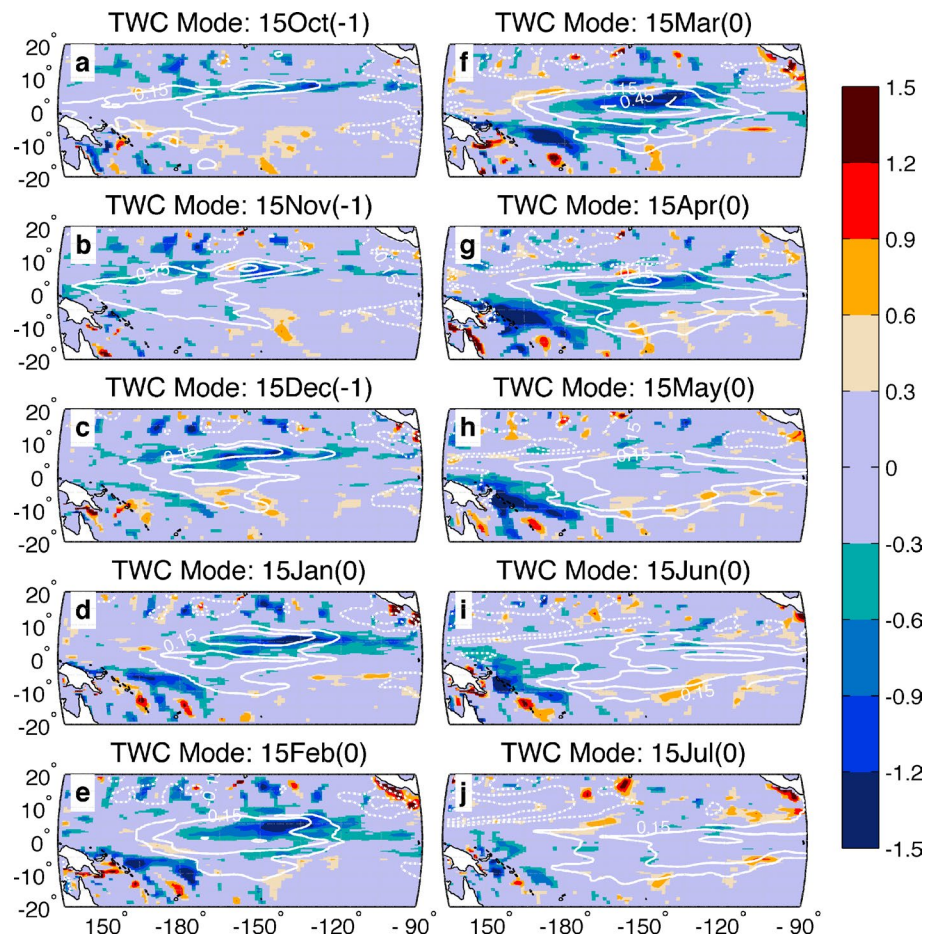
Again, to better understand the evolution of these fields, particularly of the subsurface temperature anomalies, we examine the corresponding evolution of the implied vertically-integrated meridional mass transport based upon the curl of the wind stress anomalies and vortex stretching (Fig. 11). During late boreal fall and early boreal winter (October–December), negative wind stress curl is found across much of the central and eastern off-equatorial North Pacific, where it is roughly co-located with the off-equatorial subsurface temperature anomalies centered on 5°N , suggesting that these subsurface temperature anomalies are being generated by the vertical circulation features that accompany this curl. By December (Fig. 11c), however, negative wind stress curl—along with the implied equatorward mass transport—reaches the equator and induces a regional charging of the equatorial Pacific co-located with the establishment and eastward extension of the equatorial heat content maxima. During late boreal winter (January–March) the equatorward mass transport (south of 10°N)

increases and expands over the entire central and eastern Pacific (Fig. 11d–f). Concurrently, the underlying subsurface temperature anomalies intensify, both along the equator and off of it, such that by March there exists substantial subsurface heat content anomalies representative of a charged equatorial Pacific (Fig. 11f).

Moving into the middle of boreal spring, the equatorward mass transport in the North Pacific and accompanying charging of the equatorial Pacific begin to weaken along with the overlying wind stress anomalies, although it is still apparent (Fig. 11g). In response, the subsurface temperature anomalies extend eastward, reaching the far eastern equatorial Pacific (cf. the eastward extent of the 0.15°C and 0.3°C isotherms along the equator in Fig. 11g, h). By May–July the wind stress fields and associated meridional mass transport dissipates across most of the basin. In addition, the core of the subsurface temperature anomalies have now shifted eastward (cf. the eastward extent of the 0.45°C isotherms along the equator in Fig. 10h–j) and are centered in the eastern equatorial Pacific between 150°W and 90°W .

Based upon this analysis, wind stress anomalies associated with the TWC mode induce substantial equatorial and off-equatorial subsurface temperature anomalies via meridional and vertical circulations respectively. To

Fig. 11 Same as Fig. 8 except now for the evolution of the implied vertically-integrated meridional velocity component concurrent with and following wind stress variations associated with the TWC mode of variability as represented by the time-series for the second leading mode of boreal winter τ^x variability



see how the equatorial subsurface temperature anomalies evolve, we once again examine these anomalies along an equatorial transect of the Pacific (Fig. 12). Prior to boreal winter (October), there is a weak subsurface dipole across the Pacific with warm (cold) water anomalies found over the western (far eastern) portion of the basin (Fig. 12a). As boreal winter begins and the surface wind stress anomalies intensify, the positive subsurface temperature anomalies intensify and shift eastward along the thermocline (Fig. 12c). By late boreal winter the core of these anomalies is situated at $\sim 150^\circ\text{W}$ (Fig. 12d, e), equivalent to the longitude of strongest charging (cf. Fig. 11d, e), with substantial warm water anomalies ($>1.0^\circ\text{C}$) extending from 180° to 120°W , co-located with the implied equatorward mass transport in response to both the weakening of the off-equatorial trades (west of 150°W) and combined weakening of the off-equatorial trades and strengthening of the equatorial easterlies (east of 150°W). As with the ENSO-related discharge, these anomalies remain relatively stationary through the 3-month period ending in March (Fig. 12f). However, starting in April—concurrent with the time when the TWC-related wind stress anomalies, along with the wind stress forcing of the meridional mass transport,

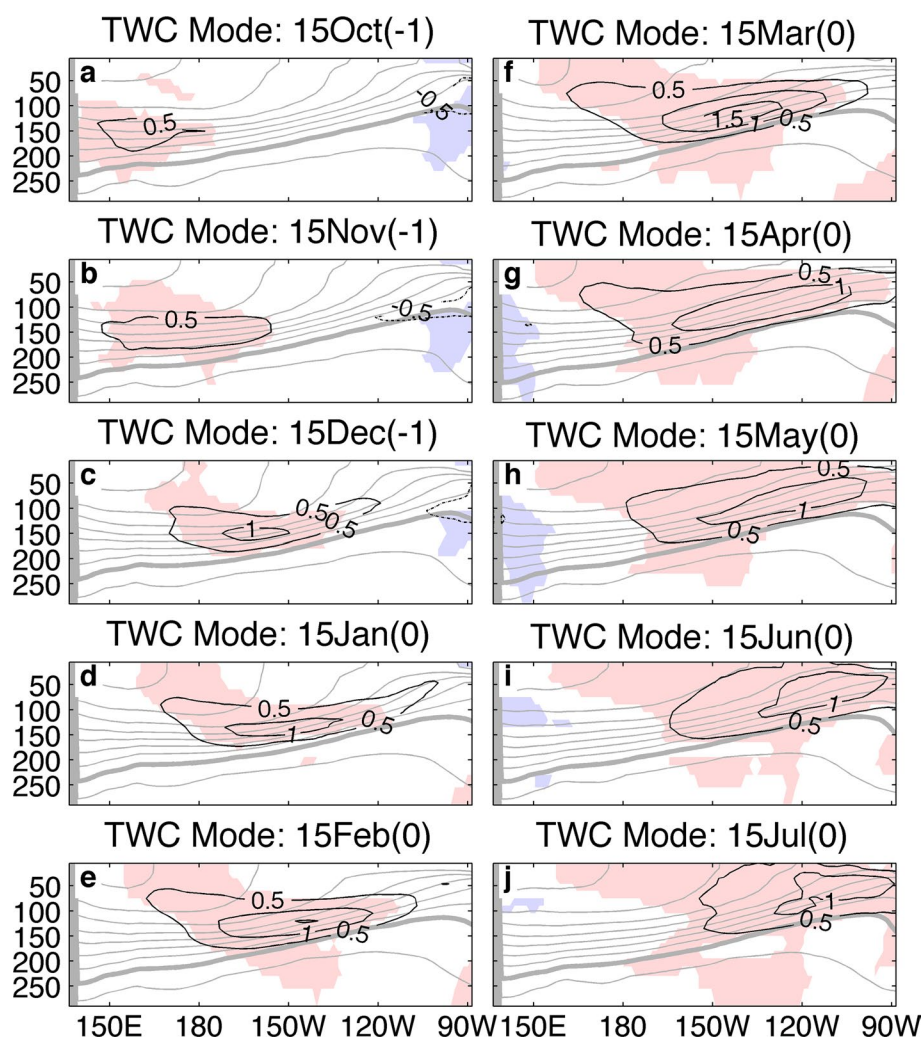
begins to dissipate—the core warm water anomaly extends eastward along the shoaling thermocline, eventually reaching the eastern equatorial Pacific (120°W) approximately 2 months later (i.e. by June—Fig. 12g–i).

Given its similarities to the structure, timing, and diagnostics of the well-known ENSO-related discharge process, we argue that the evolution of the equatorial subsurface temperature anomalies associated with this mode of tropical Pacific wind stress variability represents a charging of the equatorial warm water volume, which in turn serves as a precursor to the subsequent warming of the eastern equatorial Pacific SSTs and the onset phase of positive ENSO events. Below we synthesize these results and show how these two modes (the ENSO mode and TWC mode) of variability relate to one another.

3.2.3 Co-evolution

To start, we look at the time evolution of the convergence and divergence of off-equatorial meridional mass transport (Fig. 13, color shading) responsible for producing charging (i.e. positive heat content anomalies) and discharging (i.e. negative heat content anomalies), respectively,

Fig. 12 Same as Fig. 9 except now for the evolution of the surface and subsurface temperature anomalies along the equatorial Pacific concurrent with and following wind stress variations associated with the TWC mode of variability as represented by the time-series for the second leading mode of boreal winter τ^x variability



along the equator (Fig. 13, contours). For the ENSO mode (Fig. 13a), significant basin-wide positive subsurface heat content anomalies are found around 10 months prior to the mature ENSO events themselves (i.e. ~Month -10). The anomalies intensify and migrate eastward, establishing the characteristic subsurface temperature dipole approximately 5 months before the mature stage of the ENSO event. At approximately the same time, the discharge process starts with large divergence of meridional mass transport over the western equatorial Pacific. Both features intensify over the course of the next 3–5 months. During the mature stage of the ENSO event [~Month -2 through Month 0, equivalently Nov(-1)–Jan(0)], the leading edge of the negative subsurface heat content anomalies start to expand eastward in response to the discharge process during the preceding months. By the end of boreal winter, the discharge begins to weaken across most of the basin although remnants are found over the western equatorial Pacific that extend into late boreal spring. The negative subsurface heat content anomalies, however, continue expanding eastward such that

by the following boreal fall (~Month 8–10) they are centered around 150°W and extend from 180° to 105°W, representing a fully discharged equatorial Pacific. It should be noted, however, that no subsequent ENSO events (statistically) develop during this time, or even over the course of the next year (as evidenced by the absence of either a heat-content dipole or significant wind stress induced charging).

For the TWC mode (Fig. 13b), there are no substantial positive heat content anomalies (>0.3 °C) along the central equatorial Pacific prior to the boreal winter development of the TWC anomalies themselves, although some do develop over the far eastern equatorial Pacific during the prior boreal spring/summer. Starting at this same time (~Month -8), there is a period of relatively weak convergence of meridional mass transport (i.e., charging) near the dateline and a possible corresponding development of positive heat content anomalies over the western equatorial Pacific (as represented by the 0.15 °C isotherm). However, substantial charging does not begin until ~Month -2 [i.e. November(-1)], which subsequently lasts until early

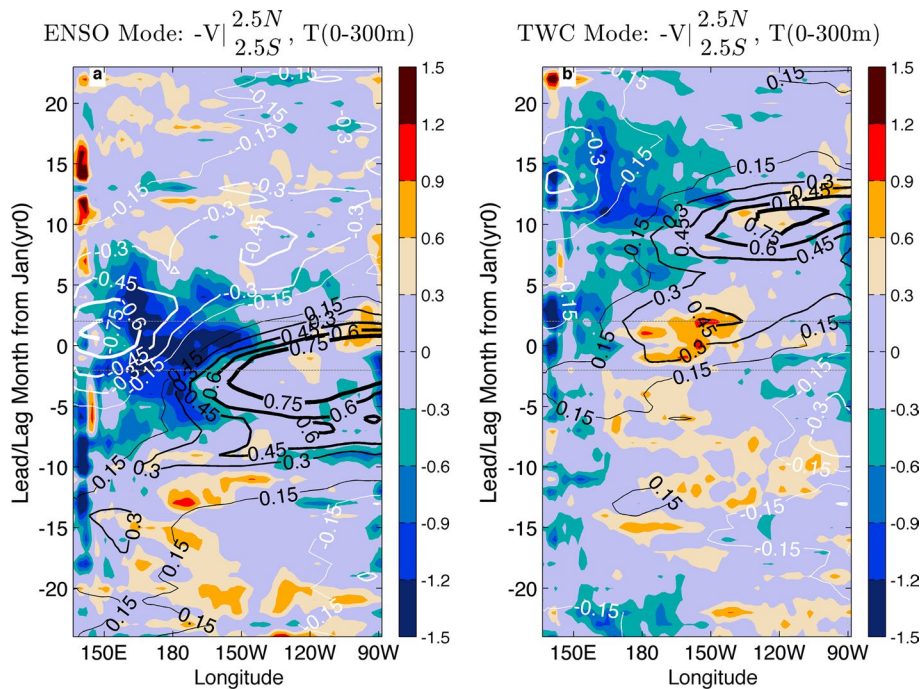


Fig. 13 a Time (y-axis)/Longitude(x-axis) plot of ocean/atmosphere anomalies along and near the equatorial Pacific prior to and following wind stress variations associated with the ENSO mode of variability. *Shading* monthly-mean implied meridional transport convergence along the equator computed from the sum of the *equatorward* components of the vertically-integrated meridional velocities (V) averaged between 2°N – 3°N and between 2°S – 3°S derived from Eq. 1 and regressed against the time-series for the leading mode of boreal winter τ^x variability. Positive values represent longitudes/times with implied equatorial convergence or charging. Minimum shading is $\pm 0.3 \text{ m}^2 \text{ s}^{-1}$; shading interval is $0.3 \text{ m}^2 \text{ s}^{-1}$. *Contours* monthly-mean $T(0\text{--}300 \text{ m})$ anomalies ($^{\circ}\text{C}$) averaged between 2°S – 2°N and

regressed against the time-series for the leading mode of boreal winter τ^x variability. Contour interval is $0.15 \text{ }^{\circ}\text{C}$; minimum contour is $\pm 0.15 \text{ }^{\circ}\text{C}$; black (white) contours indicate positive (negative) anomalies. Monthly values centered on 30-day window with '0' representing the 30-day window centered on January 15. For orientation, horizontal grey lines represent the Nov.-Mar. period concurrent with the τ^x time-series itself—see text for details. **b** Same as **a** except for implied monthly-mean equatorial convergence and $T(0\text{--}300 \text{ m})$ anomalies associated with the TWC mode of variability as represented by the time-series for the second leading mode of boreal winter τ^x variability

boreal spring. In response, lagged positive subsurface heat content anomalies start to develop and intensify, as well as expand eastward such that by the end of boreal winter (\sim Month 3), the subsurface heat content anomalies are collocated with the region of greatest charging. After the cessation of the charging in boreal spring, the subsurface heat content anomalies shift eastward such that by the following boreal fall/winter these subsurface heat content anomalies are centered in the central/eastern equatorial Pacific, where they subsequently intensify; in addition negative heat content anomalies develop over the far western Pacific in response to boreal winter discharge in this region. These two signatures (the boreal winter subsurface heat content dipole and western/central Pacific discharge in Months 10–13 following the TWC mode) are indicative of a positive ENSO event during this time (cf. Month -2 through Month $+2$ of the ENSO mode).

Indeed, while only implied up to this point, it should be noted that there is a robust correlation between the TWC-related τ^x PC time-series with the ENSO-related τ^x

PC time-series the following year ($r = 0.59$). This result is to be expected given the similarity of the TWC-related fields to known oceanic and atmospheric precursors to ENSO events (highlighted in the Sect. 1). By construction, the ENSO- and TWC-mode time-series are uncorrelated with one another at concurrent times. In addition, though, there is no significant correlation between the ENSO-related τ^x PC time-series and the TWC-related τ^x PC time-series the following year ($r = -0.09$). These results suggest TWC-related wind stress fields elucidated here are not part of the ENSO cycle, as evidenced by the absence of any wind stress induced equatorial divergence (and hence implied discharge) in Months 10–12 of Fig. 13a (even given the discharged state of the equatorial Pacific itself). Instead the TWC-related wind stress fields appear to serve as a separate mechanism for generating a “charged” (as well as “discharged”) equatorial Pacific that can subsequently induce the onset of warm (cold) ENSO events, which mature the following boreal winter.

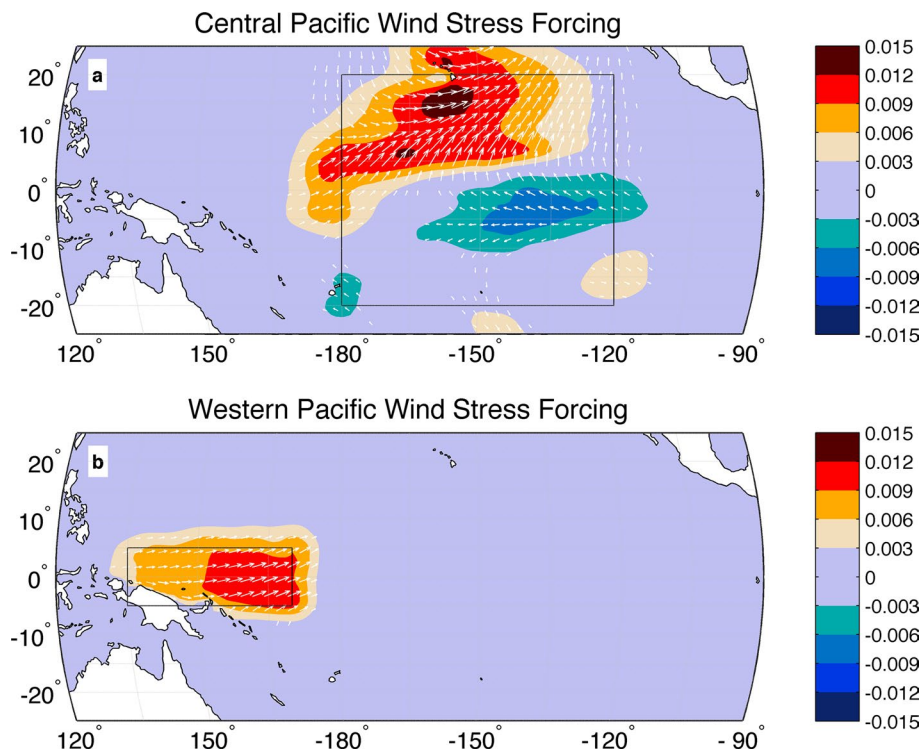


Fig. 14 Regional seasonal-mean wind-stress anomalies used to force a high-resolution dynamical ocean model centered on the tropical Pacific basin. **a** Shading Central Pacific regional zonal wind stress forcing derived from the seasonal-mean (Jan–Mar) τ^x anomalies regressed against the concurrent time-series for the second leading mode of boreal winter τ^x variability. Contour interval is 0.003 (N m^{-2}); minimum contour is ± 0.003 (N m^{-2}). Inside the box, the

full values are applied; at the edge of the box a Gaussian smoothing with a 10° window is used. Vectors full Central Pacific regional wind stress forcing derived from the seasonal-mean wind stress anomalies (N m^{-2}) regressed against the τ^x time-series. Only substantial ($|\tau| < 0.003$) anomalies are shown. **b** Same as **a** except for Western Pacific regional wind stress forcing

One final question to address is whether the TWC-related T (0–300 m) evolution in Fig. 13 could arise from western equatorial wind stress anomalies and not the central equatorial and off-equatorial anomalies (via their curl) as discussed throughout. To compare the response of the equatorial Pacific subsurface temperatures to each, we follow the experimental method employed in Anderson et al. (2013a, b). Specifically we isolate the western equatorial Pacific wind stress anomalies and the central equatorial and off-equatorial Pacific wind stress anomalies (Fig. 14) and use them to force a high-resolution ocean general circulation model (Perez and Kessler 2009) centered on the equatorial Pacific basin, using a ramp-up/ramp-down technique in which the regional forcings are added to the climatological fields and persisted for the period December–March. The ocean model is then allowed to evolve over the next 3 months with only climatological forcing. As in Anderson et al. (2013a, b), three different initializations are used to reduce mesoscale variations associated with tropical instability waves. Anomalies are obtained by subtracting the

regionally forced simulation fields from the control (i.e. climatologically forced) simulation fields.

Results indicate that the western equatorial Pacific wind stress anomalies produce subsurface temperature anomalies in the model that rapidly propagate to the eastern equatorial Pacific as Kelvin waves (McCreary 1976); the fast propagation speed associated with these waves allows the core anomalies to reach the eastern equatorial Pacific within approximately 2 months (Fig. 15b, contours). By contrast, the subsurface temperature anomalies induced by the central equatorial and off-equatorial wind stress anomalies in the model (Fig. 15a, contours) show slow eastward propagation speeds similar to those found in the ocean analysis (Fig. 15a, color shading), suggesting that the dynamic processes active in the observationally-constrained ocean analysis are more representative of the TWC dynamics than of Kelvin wave dynamics. Indeed, this dominant influence of the central equatorial and off-equatorial Pacific wind stress anomalies, vis a vis those found over the western equatorial Pacific, mirrors similar results derived from numerical ocean analyses (Larson and Kirtman 2013).

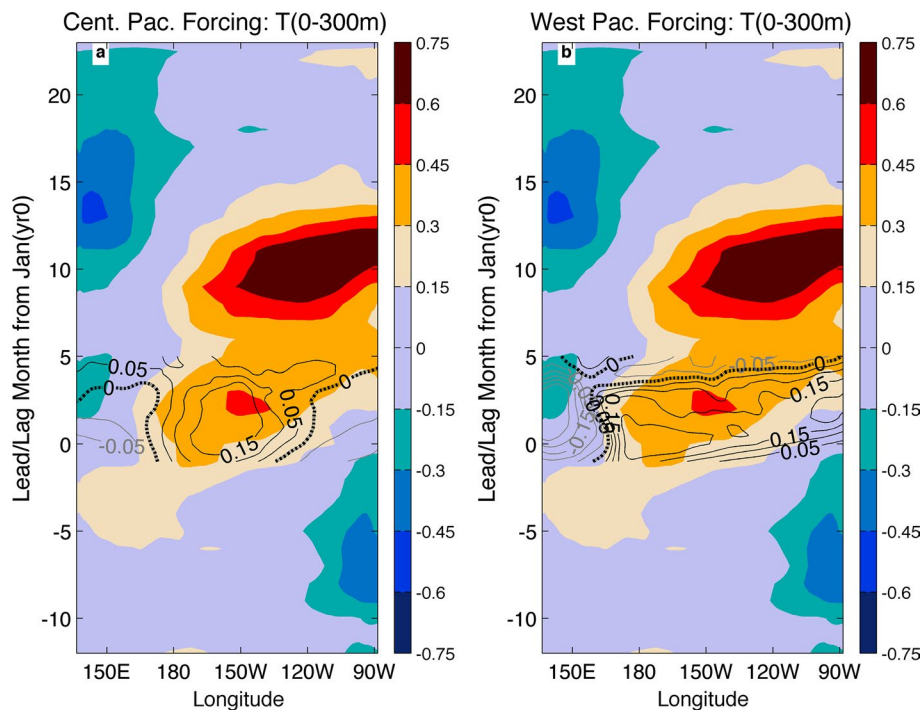


Fig. 15 **a** Time (y-axis)/Longitude (x-axis) plot of ocean anomalies along the equatorial Pacific prior to and following wind stress variations associated with the TWC mode of wind stress variability. *Shading* monthly-mean T (0–300 m) anomalies ($^{\circ}\text{C}$) averaged between 2°S – 2°N and regressed against the time-series for the second leading mode of boreal winter τ^x variability. Shading interval is 0.15°C ; minimum shading is $\pm 0.15^{\circ}\text{C}$. Monthly values centered on 30-day window with ‘0’ representing the 30-day window centered on January 15. *Contours* monthly-mean T (0–300 m) anomalies ($^{\circ}\text{C}$) averaged

between 2°S and 2°N generated by forcing a high-resolution ocean model of the tropical/subtropical Pacific basin with idealized TWC-related wind stress fields over the central Pacific only (as shown in Fig. 14a). Contour interval is 0.05°C . See text and Anderson et al. (2013a, b) for details. **b** *Shading* same as in **a**. *Contours* monthly-mean T (0–300 m) anomalies ($^{\circ}\text{C}$) averaged between 2°S and 2°N generated by forcing a high-resolution ocean model forced with idealized TWC-related wind stress fields over the equatorial western Pacific only (as shown in Fig. 14b)

4 Summary

Empirical and dynamical links between extratropical atmospheric circulations—particularly over the North Pacific during boreal winter—and the onset of mature ENSO events have been the subject of numerous investigations over the years (see the Sect. 1 and references therein). A predominant focus has been on the modification of air–sea interactions induced by these circulations, which through their coupling at the surface can modify the dynamic and thermodynamic structure of the equatorial ocean/atmosphere system and the onset of ENSO events. Less well understood however, is how these circulations can influence the subsurface temperatures of the equatorial Pacific, despite the recognition that subsurface heat content variations are a fundamental precursor to mature ENSO events and that subsurface heat content variations are influenced by wind stress variations off the equator as well as along it. In this paper, we begin to advance our understanding of this relatively unexplored, but potentially more direct, pathway linking extratropical atmospheric circulations to the initiation of

ENSO events via a “trade-wind charging” of equatorial heat content.

Following the lead of previous research investigating tropical-atmosphere modes of near-surface variability (i.e. Larson and Kirtman 2013) we first perform an EOF analysis to find the leading modes of zonal-wind stress variability over the central and eastern tropical/subtropical Pacific. The leading mode of variability corresponds well with year-to-year variations in the ENSO system, both temporally and spatially, and is characterized by a monopole in the zonal-wind structure centered on the dateline and equator that decreases towards higher latitudes, accompanied by a monopole (east/west dipole) in the equatorial surface (subsurface) temperatures. The implied vertically-integrated meridional mass transport associated with the meridional gradient in zonal wind stress in turn results in a discharging of the equatorial heat content across the entire western half of the Pacific (given the sign convention used here). In response, subsurface temperature anomalies develop and intensify over the western equatorial Pacific during the mature stage of the ENSO event, however they remain relatively stationary until the decay of the ENSO

event itself during the following boreal spring, at which point the subsurface temperature anomalies extend eastward along the thermocline and (again, given the sign convention used here) produce a fully discharged equatorial Pacific by the following boreal summer.

While many of these features have been documented previously (e.g. Jin 1997; Meinen and McPhaden 2000; Clarke et al. 2007; Ishida et al. 2008; Kug et al. 2003; Kao and Yu 2009; Ren and Jin 2013; Wen et al. 2014), we present them here to provide a basis for understanding similar behavior associated with the second leading mode of tropical Pacific wind stress variability. This second leading mode is characterized by westerly (easterly) wind stress anomalies over the western (eastern) equatorial Pacific, as well as off-equatorial westerly anomalies across much of the tropical/subtropical North Pacific, representative of a weakening of the northeasterly trades in this region (given the sign convention used here). This wind stress anomaly structure corresponds well with similar patterns associated with meridional variations in SSTs across the tropical North Pacific (i.e. the Pacific Meridional Mode) and is functionally equivalent. However, as shown here it is also associated with zonally extensive subsurface temperature anomalies over the central Pacific from 165°E to 135°W and 5°S to 5°N, representative of a “charged” equatorial Pacific. By extension we argue here that these wind stress fields not only influence the underlying SST fields (as investigated by others—see Sect. 1 and references therein) but also the subsurface temperature fields; hence here we refer to it as the trade-wind charging (TWC) mode.

Indeed, the implied vertically-integrated meridional transport associated with the curl of the TWC-related wind stress anomalies results in a charging of the equatorial heat content across the central and eastern Pacific (again, given the sign convention used here). In response, subsurface temperature anomalies develop and intensify over the central equatorial Pacific during the concurrent boreal winter. As with the ENSO subsurface temperature anomalies, these remain relatively stationary until the following boreal spring when the wind stress fields themselves dissipate. At that point, the subsurface temperature anomalies extend eastward along the thermocline and shoal during boreal summer, resulting in a warming of the SSTs in the eastern equatorial Pacific and the onset of a (positive) ENSO event that matures the following boreal winter. We note that given the linear statistics used here the process is not sign dependent and as such the reverse evolution tends to follow boreal winters with negative TWC-related zonal wind stress anomalies.

Given that for each mode of tropical Pacific wind stress variability, variations in the equatorial and off-equatorial trade winds over the Pacific appear to be dynamically linked via their curl to subsurface ocean temperatures, we

consider each to represent a separate mechanism for charging and discharging the equatorial Pacific heat content. However, the ENSO-related discharging (charging) of the equatorial Pacific appears to result in the initiation of the decay phase of the positive (negative) ENSO event itself, and possibly the cyclical initiation of an ENSO event of opposite sign (although no such cyclical behavior is found in our results). By contrast, the TWC-related charging (discharging) appears to result in the initiation of the onset phase of a positive (negative) ENSO event, which subsequently matures by the following boreal winter. While beyond the scope of this paper, these results suggest that for the purpose of predicting ENSO events, non-ENSO related charging and discharging (via variations in the equatorial and off-equatorial trade winds) may be important in influencing the growth of subsequent ENSO events. That said, it is recognized that the TWC mode isolated here is by no means the only initiator of ENSO events and that other initiating mechanisms can contribute—in isolation or jointly—to the onset of any particular event (e.g. Neelin et al. 1998). Further, based upon two sets of seemingly contradictory results in the literature—namely that: (1) NPO-related extratropical forcing of ENSO may preferentially induce the onset of central Pacific (CP) ENSO events (Yu and Kim 2011; Yu et al. 2012; Vimont et al. 2014) or alternatively Eastern Pacific (EP) ENSO events (Anderson et al. 2013a, b; Larson and Kirtman 2014); and (2) charged heat content anomalies along the equator may (Vimont et al. 2014; McPhaden 2012; Kumar and Hu 2014) or may not (Wen et al. 2014; Ren and Jin 2013) preferentially induce the onset of EP ENSO events relative to CP ENSO events—the TWC mode and its concomitant changes in subsurface temperatures also may be important in influencing the structural characteristics (i.e., the so-called diversity) of the subsequent ENSO events, although again such an investigation is beyond the scope of this paper.

Acknowledgments This work was supported by the Department of Energy (DE-SC0004975 to B.T.A.). This research was also carried out in part under the auspices of the Cooperative Institute of Marine and Atmospheric Studies (CIMAS), a Cooperative Institute of the University of Miami and the National Oceanic and Atmospheric Administration (NOAA), cooperative agreement #NA10OAR4320143 (R.C.P.). Additional support was provided by NOAA’s Atlantic Oceanographic and Meteorological Laboratory (R.C.P.).

References

- Alexander MA et al (2002) The atmospheric bridge: the influence of ENSO teleconnections on air–sea interaction over the global ocean. *J Clim* 15:2205–2231
- Alexander MA, Vimont DJ, Chang P, Scott JD (2010) The impact of extratropical atmospheric variability on ENSO: testing the seasonal footprinting mechanism using coupled model experiments. *J Clim* 23:2885–2901

- Anderson BT (2003) Tropical Pacific sea-surface temperatures and preceding sea-level pressure anomalies in the subtropical North Pacific. *J Geophys Res* 108: Art No 4732
- Anderson BT (2004) Investigation of a large-scale mode of ocean-atmosphere variability and its relation to tropical Pacific sea surface temperature anomalies. *J Clim* 17:1089–4098
- Anderson BT, Maloney E (2006) Interannual tropical Pacific sea-surface temperatures and preceding sub-tropical North Pacific sea level pressure anomalies in the NCAR CCSM2.0. *J Clim* 19:998–1012
- Anderson BT, Perez R, Karspeck A (2013a) Triggering of El Niño onset through the trade-wind induced charging of the equatorial Pacific. *Geophys Res Lett*. doi:[10.1002/grl.50200](https://doi.org/10.1002/grl.50200)
- Anderson BT, Furtado JC, Di Lorenzo E, Cobb K (2013b) Extratropical forcing of El Niño/Southern Oscillation asymmetry. *Geophys Res Lett*. doi:[10.1002/grl.50951](https://doi.org/10.1002/grl.50951)
- Balmaseda MA, Vidard A, Anderson DLT (2008) The ECMWF ocean analysis system: ORA-S3. *Mon Weather Rev* 136:3018–3034
- Balmaseda MA, Mogensen K, Weaver AT (2013) Evaluation of the ECMWF ocean reanalysis system ORAS4. *Q J R Meteorol Soc* 139:1132–1161
- Barnett TP (1985) Variations in near-global sea level pressure. *J Atmos Sci* 42:478–501
- Barnett TP et al (1988) On the prediction of the El Niño of 1986–1987. *Science* 241:92–196
- Barnett TP et al (1999) Interdecadal interactions between the tropics and midlatitudes in the Pacific basin. *Geophys Res Lett* 26:615–618
- Capotondi A, Alexander MA, Deser C (2003) Why are there Rossby wave maxima in the Pacific at 10°S and 13°N? *J Phys Ocean* 33:1549–1563
- Chan JCL, Xu JJ (2000) Physical mechanisms responsible for the transition from a warm to a cold state of the El Niño–Southern Oscillation. *J Clim* 13:2056–2071
- Chang P et al (2007) Pacific meridional mode and El Niño—Southern Oscillation. *Geophys Res Lett*. doi:[10.1029/2007GL030302](https://doi.org/10.1029/2007GL030302)
- Chiang JCH, Vimont DJ (2004) Analogous Pacific and Atlantic meridional modes of tropical atmosphere–ocean variability. *J Clim* 17:4143–4158
- Clarke AJ, Van Gorder S, Colantuono G (2007) Wind stress curl and ENSO discharge/recharge in the equatorial Pacific. *J Phys Ocean* 37:1077–1091
- Deser C, Capotondi A, Saravanan R, Phillips AS (2006) Tropical Pacific and Atlantic climate variability in CCSM3. *J Clim* 19:2451–2481
- Deser C et al (2012) ENSO and Pacific decadal variability in the Community Climate System Model Version 4. *J Clim* 25:2622–2651
- Ely LL et al (1993) A 5000-year record of extreme floods and climate-change in the Southwestern United States. *Science* 262:410–412
- Gershunov A, Barnett TP (1998) ENSO influence on intraseasonal extreme rainfall and temperature frequencies in the contiguous United States: observations and model results. *J Clim* 11:1575–1586
- Gu D, Philander SGH (1997) Interdecadal climate fluctuations that depend on exchanges between the tropics and extratropics. *Science* 275:805–807
- Ishida A, Kashido Y, Hosoda S, Ando K (2008) North-south asymmetry of warm water volume transport related with El Niño variability. *Geophys Res Lett*. doi:[10.1029/2008GL034858](https://doi.org/10.1029/2008GL034858)
- Jin F-F (1997) An equatorial ocean recharge paradigm for ENSO 1 Conceptual model. *J Atmos Sci* 54:811–829
- Jin F-F, Neelin JD, Ghil M (1994) El Niño on the Devil’s staircase—annual subharmonic steps to chaos. *Science* 164:70–72
- Kao H-Y, Yu J-Y (2009) Contrasting eastern-Pacific and central-Pacific types of ENSO. *J Clim* 22:615–632
- Kidson JE (1975) Tropical eigenvector analysis and the southern oscillation. *Mon Weather Rev* 103:187–196
- Kiladis GN, Diaz HF (1989) Global climatic anomalies associated with extremes in the Southern Oscillation. *J Clim* 2:1069–1090
- Kug J-S, Kang I-S, An S-I (2003) Symmetric and antisymmetric mass exchanges between the equatorial and off-equatorial Pacific associated with ENSO. *J Geophys Res*. doi:[10.1029/2002JC001671](https://doi.org/10.1029/2002JC001671)
- Kumar A, Hoerling MP (1998) Annual cycle of Pacific–North American seasonal predictability associated with different phases of ENSO. *J Clim* 11:3295–3308
- Kumar A, Hu Z-Z (2014) Interannual and interdecadal variability of ocean temperature along the equatorial Pacific in conjunction with ENSO. *DOI, Clim Dyn*. doi:[10.1007/s00382-013-1721-0](https://doi.org/10.1007/s00382-013-1721-0)
- Larson S, Kirtman B (2013) The Pacific meridional mode as a trigger for ENSO in a high-resolution coupled model. *Geophys Res Lett*. doi:[10.1002/grl50571](https://doi.org/10.1002/grl50571)
- Larson S, Kirtman B (2014) Assessing Pacific meridional mode forecasts and its role as an ENSO precursor and predictor in the North American multi-model ensemble. *J Clim*. doi:[10.1175/JCLI-D-14-00055.1](https://doi.org/10.1175/JCLI-D-14-00055.1)
- Li T (1997) Phase transition of the El Niño–Southern Oscillation: a stationary SST mode. *J Atmos Sci* 54:2872–2887
- Linkin ME, Nigam S (2008) The North Pacific Oscillation–West Pacific teleconnection pattern: mature-phase structure and winter impacts. *J Clim* 21:1979–1997
- Lynse J, Chang P, Giese B (1997) Impact of the extratropical Pacific on equatorial variability. *Geophys Res Lett* 24:2589–2592
- McCreary J (1976) Eastern tropical ocean response to changing wind systems—with application to El Niño. *J Phys Oceanogr* 6:632–645
- McPhaden MJ (2003) Tropical Pacific Ocean heat content variations and ENSO persistence barriers. *Geophys Res Lett*. doi:[10.1029/2003GL016872](https://doi.org/10.1029/2003GL016872)
- McPhaden MJ (2012) A 21st century shift in the relationship between ENSO SST and warm water volume anomalies. *Geophys Res Lett*. doi:[10.1029/2012GL051826](https://doi.org/10.1029/2012GL051826)
- Meinen CS, McPhaden MJ (2000) Observations of warm water volume changes in the equatorial Pacific and their relationship to El Niño and La Niña. *J Clim* 13:3551–3559
- Neelin JD et al (1998) ENSO theory. *J Geophys Res* 103:14261–14290
- Newman M, Alexander MA, Scott JD (2011) An empirical model of tropical ocean dynamics. *Clim Dyn* 37:1823–1841
- Penland C (1996) A stochastic model of IndoPacific sea surface temperature anomalies. *Phys D* 98:534–558
- Penland C, Sardeshmukh PD (1995) The optimal growth of tropical sea surface temperature anomalies. *J Clim* 8:1999–2024
- Perez RC, Kessler WS (2009) Three-dimensional structure of tropical cells in the central equatorial Pacific Ocean. *J Phys Oceanogr* 39:27–49
- Philander SGH (1985) El Niño and La Niña. *J Atmos Sci* 42:2652–2662
- Pierce DW, Barnett TP, Latif M (2000) Connections between the Pacific ocean tropics and midlatitudes on decadal timescales. *J Clim* 13:1173–1194
- Rasmusson EM, Carpenter TH (1981) Variations in tropical sea surface temperature and surface wind fields associated with the Southern Oscillation/El Niño. *Mon Weather Rev* 110:354–384
- Reiter ER (1978) Long-term wind variability in the tropical Pacific, its possible causes and effects. *Mon Weather Rev* 106:324–330
- Ren H-L, Jin F-F (2013) Recharge oscillator mechanisms in two types of ENSO. *J Clim*. doi:[10.1175/JCLI-D-12-00601.1](https://doi.org/10.1175/JCLI-D-12-00601.1)
- Richter I et al (2013) Multiple causes of interannual sea surface temperature variability in the equatorial Atlantic ocean. *Nat Geosci* 6:43–47
- Rogers JC (1981) The north Pacific oscillation. *J Clim* 1:39–57
- Ropelewski CF, Halpert MS (1986) North American precipitation and temperature patterns associated with the El Niño/Southern Oscillation (ENSO). *Mon Weather Rev* 114:2352–2362

- Ropelewski CF, Halpert MS (1996) Quantifying Southern Oscillation–precipitation relationships. *J Clim* 9:1043–1059
- Schneider DP, Steig EJ (2008) Ice cores record significant 1940s Antarctic warmth related to tropical climate variability. *Proc Natl Acad Sci* 105:12154–12158
- Shukla J et al (2000) Dynamical seasonal prediction. *Bull Am Meteorol Soc* 81:2593–2606
- Trenberth KE (1976) Spatial and temporal variations of the Southern Oscillation. *Q J R Meteorol Soc* 102:639–653
- Trenberth KE (1997) The definition of El Niño. *Bull Am Meteorol Soc* 78:2771–2777
- Trenberth KE, Shea DJ (1987) On the evolution of the Southern Oscillation. *Mon Weather Rev* 115:3078–3096
- Trenberth KE et al (1998) Progress during TOGA in understanding and modeling global teleconnections associated with tropical sea surface temperatures. *J Geophys Res* 103:14291–14324
- van Loon HL, Shea DJ (1985) The Southern Oscillation Part IV: the precursors south of 15°S to the extremes of the oscillation. *Mon Weather Rev* 113:2063–2074
- van Loon HL, Shea DJ (1987) The Southern Oscillation Part VI: anomalies of sea level pressure on the southern hemisphere and of the Pacific sea surface temperature during the development of a warm event. *Mon Weather Rev* 115:370–379
- Vimont DJ, Battisti S, Hirst AC (2001) Footprinting, A seasonal connection between the tropics and mid-latitudes. *Geophys Res Lett* 28:3923–3926
- Vimont DJ, Wallace JM, Battisti S (2003a) The seasonal footprinting mechanism in the Pacific: implications for ENSO. *J Clim* 16:2668–2675
- Vimont DJ, Battisti S, Hirst AC (2003b) The seasonal footprinting mechanism in the CSIRO general circulation models. *J Clim* 16:2653–2667
- Vimont DJ, Alexander MA, Newman M (2014) Optimal growth of central and east Pacific ENSO events. *Geophys Res Lett*. doi:[10.1002/2014GL059997](https://doi.org/10.1002/2014GL059997)
- Walker GT, Bliss EW (1932) World Weather V. *Mem R Meteorol Soc* 4:53–83
- Wang S-Y, L'Heureux M, Chia H-H (2012) ENSO prediction one year in advance using western North Pacific sea surface temperatures. *Geophys Res Lett*. doi:[10.1029/2012GL050909](https://doi.org/10.1029/2012GL050909)
- Wen C, Kumar A, Xue Y, McPhaden MJ (2014) Changes in tropical Pacific thermocline depth and their relationship to ENSO after 1999. *J Clim*. doi:[10.1175/JCLI-D-13-00518.1](https://doi.org/10.1175/JCLI-D-13-00518.1)
- Wu S, Wu LX, Liu QY, Xie S-P (2010) Development processes of the Tropical Pacific Meridional Mode. *Adv Atmos Sci* 27:95–99
- Wyrtki K (1985) Water displacements in the Pacific and the genesis of El Niño cycles. *J Geophys Res Oceans* 90:7129–7132
- Xie S (1999) A dynamic ocean–atmosphere model of the tropical Atlantic decadal variability. *J Clim* 12:64–70
- Yu J-Y, Kim S-T (2011) Relationships between extratropical sea level pressure variations and the central Pacific and eastern Pacific types of ENSO. *J Clim*. doi:[10.1175/2010JCLI3688.1](https://doi.org/10.1175/2010JCLI3688.1)
- Yu J-Y, Lu M-M, Kim S-T (2012) A change in the relationship between tropical central Pacific SST variability and the extratropical atmosphere around 1990. *Environ Res Lett*. doi:[10.1088/1748-9326/7/3/034025](https://doi.org/10.1088/1748-9326/7/3/034025)
- Zhang L, Chang P, Ji L (2009) Linking the Pacific meridional mode to ENSO: coupled model analysis. *J Clim* 22:3488–3505
- Zheng XG, Nakamura H, Renwick JA (2000) Potential predictability of seasonal means based on monthly time series of meteorological variables. *J Clim* 13:2591–2604